JOURNAL OF GEOPHYSICAL RESEARCH, VOL. ???, XXXX, DOI:10.1029/,

Radio occultations of the Io plasma torus by *Juno* are feasible

Phillip H. Phipps,[1] Paul Withers,[1,2]

---

[1]Department of Astronomy, Boston University, Boston, Massachusetts, USA.

[2]Center for Space Physics, Boston University, Boston, Massachusetts, USA.

Abstract. The flow of material from Io's volcanoes into the Io plasma torus, out into the magnetosphere, and along field lines into Jupiter's upper atmosphere is not adequately understood. The lack of observations of spatial and temporal variations in the Io plasma torus impedes attempts to understand the system as a whole. Here we propose that radio occultations of the Io plasma torus by the *Juno* spacecraft can measure plasma densities in the Io plasma torus. We find that the line-of-sight column density of plasma in each of the three regions of the Io plasma torus (cold torus, ribbon, and warm torus) can be measured with uncertainties of 10%. We also find that scale heights describing the spatial variation in plasma density in each of these three regions can be measured with similar uncertainties. Such observations will be sufficiently accurate to support system-scale studies of the flow of plasma through the magnetosphere of Jupiter.

1. Introduction

Volcanic eruptions on the innermost Galilean satellite, Io, are the main source of plasma in Jupiter's magnetosphere. Io orbits Jupiter in the plane of the planet's rotational equator at a distance of 5.9 R_J. Volcanic activity on Io delivers neutral gas into the Jupiter system at a rate of about 1 tonne per second [e.g. *Bagenal and Delamere*, 2011]. Plasma is produced from these neutrals via electron collisions on timescales of 2–5 hours [*Smyth and Combi*, 1988; *Smyth*, 1992; *Thomas et al.*, 2004]. Plasma is also transferred into the magnetosphere as Jupiter's rapidly rotating magnetic field picks up ions from Io's ionosphere. The relative importance of these two processes is not currently known [*Thomas et al.*, 2004].

Once ionized, these particles are affected by electromagnetic forces in addition to gravitational and centrifugal forces. These forces disperse the Io-genic plasma away from Io, but do not do so uniformly in all directions. Instead, the plasma is initially confined to a torus that is centered on the centrifugal equator at Io's orbital distance (5.9 R_J), called the Io plasma torus (IPT). The centrifugal equator is the locus of points on a given field line which are located at the greatest distance from the rotation axis [*Hill et al.*, 1974; *Dessler*, 2002; *Khurana et al.*, 2004]. The torus is centered in this plane since this plane is where an ion trapped on a field line has the minimum centrifugal potential. The axis of the centrifugal equator lies between Jupiter's rotational and magnetic axes and is therefore tilted towards the magnetic axis at 200° longitude (System III). The angle between the rotational and centrifugal axes is 2/3 the angle between the rotational and magnetic axes [*Hill et al.*, 1974]. Since Jupiter's magnetic axis is 9.6 degrees from the rotational axis, the centrifugal axis that defines the plane of the IPT is tilted by 6.4 degrees from the rotational axis and 3.2 degrees from the magnetic axis [*Thomas et al.*, 2004]. The jovian magnetic field is not perfectly dipolar. Consequently, representing the centrifugal equator as a plane is an approximation. However, doing so is sufficient for many purposes.

Plasma is lost from the IPT via flux tube interchange on timescales of around 20-80 days [*Hill et al.*, 1981; *Bagenal and Delamere*, 2011]. Flux tube interchange causes plasma to drift radially outward, which distributes plasma throughout Jupiter's middle and outer magnetosphere. The dispersal of plasma from the IPT into the rest of the magnetosphere is the main process that provides plasma to the rest of Jupiter's magnetosphere. Therefore spatial and temporal variations in the IPT can ultimately affect the distribution and dynamics of plasma throughout Jupiter's entire magnetosphere [*Bonfond et al.*, 2012; *Payan et al.*, 2014].

There are several different ways in which remote sensing and in situ observations can measure conditions in the IPT. This article focuses on remote sensing observations of the IPT by radio occultations. These observations can monitor temporal and spatial variations in the density and temperature of the IPT.

A radio occultation occurs when an object, here the IPT, comes between the transmitter and receiver of a radio signal. Properties of the radio signal are affected by the radio signal's propagation through the plasma in the torus. Refraction of the radio signal as it passes through the plasma of the IPT causes a change in the frequency of the received signal due to the Doppler effect. The line-of-sight integrated plasma density, also known as the total electron content (TEC), of the IPT can be determined from the measured shift in the received frequency [e.g. *Withers et al.*, 2014]. The most suitable scenario for a radio occultation observation of the IPT involves a spacecraft in a polar orbit around Jupiter with periapsis within Io's orbit. A polar orbit ensures that the line of sight between the spacecraft and Earth is approximately parallel to the torus equator and sweeps through the entire cross-section of the IPT. A periapsis within Io's orbit ensures that the line of sight between the spacecraft and Earth passes through the torus once, not twice, which simplifies analysis.

The only spacecraft currently operational at Jupiter, *Juno*, has such an orbit. Launched on 5 August 2011, *Juno* entered orbit around 4 July 2016 and orbits with a near-polar inclination. The *Juno* orbiter is the first spacecraft to operate in the outer solar system using solar power and the first to have a polar orbit around Jupiter [*Bagenal et al.*, 2014]. The nominal *Juno* mission lifetime is 37 orbits. Four of these orbits are dedicated to spacecraft checkout and instrument commissioning, leaving 33 planned science orbits [*Connerney et al.*, 2016]. *Juno*'s perijove is at equatorial latitudes and 1.06 R_J, which is about 4300 km above the planet's cloud-tops. Opportunities to conduct radio occultation observations of the IPT occur once per orbit. Prior to orbit insertion, *Juno* planned to conduct most of its mission in a 14-day orbit. Due to anomalies encountered early in its orbital mission, the spacecraft may instead remain in a 53-day orbit for a considerable time. The main findings of this article are not affected by the length of the orbital period as long as *Juno* has a near-polar orbit with periapsis inside Io's orbit, which is true at the time of writing and likely to remain true until the end of the mission. The only significant effect of changes from the planned orbital period is in temporal resolution. Measurements will be possible once per orbital period, so every 53 days instead of every 14 days.

A major goal of the *Juno* mission is to map Jupiter's gravitational and magnetic fields [*Bagenal et al.*, 2014]. Analysis of these observations will improve understanding of the planet's interior structure and the properties of the magnetosphere out of the equatorial plane. The gravitational mapping requires continuous radio tracking from Earth, so the *Juno* orbit is designed such that *Juno* is never occulted from view by Jupiter itself. The *Juno* project plans to conduct radio tracking on about 24 orbits [*Tommei et al.*, 2015], which means that radio occultations may be feasible on those 24 orbits. With only two previous radio occultations of the IPT, the 24 possible *Juno* occultations offer an order of magnitude increase in the number of observations and unprecedented opportunities to explore spatial and temporal variability in the IPT. This set of occultations will sample the full range of System III longitudes and the full range of positions relative to Io along its orbit, but only a narrow range of local times. Due to the small angular separation of Earth and the Sun as seen from Jupiter, all occultations will be near noon local time.

The aims of this article are to evaluate the feasibility of measuring properties of the IPT with radio occultations conducted by the *Juno* spacecraft, to estimate the likely accuracy of such observations, and to assess the contributions that such measurements could make towards key science questions concerning the IPT and its role in Jupiter's magnetosphere.

Section 2 describes the IPT. Section 3 discusses the concept of a radio occultation and relevant capabilities of *Juno*. Section 4 explores radio occultations of the IPT using a simple model. Section 5 uses a more sophisticated model of the torus to determine the accuracy with which key torus properties can be measured. Section 6 discusses how plasma temperature and density can be obtained from the measured properties. Section 7 presents the conclusions of this work.

2. Overview of observations of the Io plasma torus

The IPT can be observed in a variety of ways, including ground-based optical and infrared measurements [*Brown*, 1995; *Schneider and Trauger*, 1995], spacecraft in situ measurements [*Judge and Carlson*, 1974; *Carlson and Judge*, 1975; *Bagenal and Sullivan*, 1981; *Bagenal et al.*, 1997], spacecraft ultraviolet (UV) measurements [*Steffl et al.*, 2004a, b], and spacecraft radio occultation experiments [*Eshleman et al.*, 1979a; *Levy et al.*, 1981; *Bird et al.*, 1992].

Ground-based optical and infrared observations can measure the composition, density, and temperatures of plasma within the IPT [*Kupo et al.*, 1976; *Pilcher and Morgan*, 1979; *Brown*, 1995; *Schneider and Trauger*, 1995]. The intensities of species-specific emission lines indicate the composition of the plasma. Electron density in the IPT can be determined from the intensity ratio of S^+ emission lines at 6717 and 6731 Å or the intensity ratio of O^+ emission lines at 3726 and 3729 Å [*Brown*, 1976]. The electron temperature can be determined from intensity ratios of other pairs of S^+ lines and the perpendicular ion temperature can be determined from the width of the S^+ 6731 Å line [*Brown*, 1976]. The brightest emissions from the IPT are sodium D-line emissions due to resonant scattering of solar radiation by neutral sodium, although their behavior is different from typical torus plasma since they are neutral. We can expect the sodium emission to be a tracer of the neutrals but not of the ions. These emissions are often used as proxy measurements for the main constituents of the IPT, ionized sulfur and oxygen. Many ground-based surveys of spatial and temporal variability in the IPT have been conducted [e.g. *Brown*, 1995; *Schneider and Trauger*, 1995; *Mendillo et al.*, 2004a; *Nozawa et al.*, 2004, 2005, 2006; *Yoneda et al.*, 2009, 2010, 2013].

Valuable observations of the IPT were made by *Voyager 1* during its flyby in March 1979 [*Bagenal and Sullivan*, 1981] and *Galileo* during its orbital tour in 1995–2003 [*Bagenal et al.*, 1997]. Each spacecraft was equipped with an ultraviolet spectrometer (UVS) that covered 400–1800 Å and an in situ plasma instrument (PLS). The UVS experiments were able to measure electron density and temperature, ion temperature perpendicular to the magnetic field, and composition. The PLS experiments were able to measure plasma density, velocity, and composition [*Bagenal*, 1994; *Thomas et al.*, 2004]. Due to degeneracies in the interpretation of observations from each instrument, both remote sensing UVS measurements and in situ PLS measurements were necessary to map the composition of the torus completely. In situ measurements by *Voyager 1* [*Bagenal and Sullivan*, 1981] and *Galileo* [*Bagenal et al.*, 1997] mapped the spatial extent of the IPT. They found that the IPT is centered at the orbital distance of Io, 5.9 R_J, and has widths of about 2 R_J in, and 1 R_J perpendicular to, the plane of the centrifugal equator. The Cassini Ultraviolet Imaging Spectrograph (UVIS) also observed the IPT during Cassini's Jupiter flyby in 2000–2001 [*Steffl et al.*, 2004a, b].

The spatial distribution of plasma in the IPT has also been mapped by active remote sensing experiments on spacecraft in the Jupiter system. Prior to *Juno*, radio occultations through the IPT have been conducted twice, once by *Voyager 1* [*Eshleman et al.*, 1979a; *Levy et al.*, 1981; *Campbell and Synnott*, 1985] and later by *Ulysses* [*Bird et al.*, 1992, 1993]. These observations provided a time series of measurements of the TEC in the IPT between the spacecraft and Earth. In combination with knowledge of the spacecraft trajectory, these TEC measurements constrained spatial variations in the local electron density within the IPT.

From these observations, a general picture of the IPT has been developed. From *Voyager 1* measurements, *Bagenal and Sullivan* [1981] found that the torus can be divided into three different regions: the cold torus, ribbon, and warm torus. The innermost region, centered at 5.2 R_J, is the cold torus. In the cold torus, densities fall off with height above the centrifugal equator with a scale height of 0.1 R_J, which is relatively small. The cold torus peaks at around 5.23 R_J and extends from 4.9 R_J to 5.5 R_J and has a characteristic density of $\sim$1000 cm^{-3}. Its composition is mostly S$^+$ ions with smaller amounts of O$^+$ ions present. In the cold torus, the electron temperature $T_e \approx$ 1–2 eV and the ion temperature $T_i \approx$ 1–4 eV. Beyond the cold torus lies the ribbon, whose center is at a distance of 5.6 R_J. It has a scale height of 0.6 R_J and extends from 5.5–5.7 R_J. The ribbon has a high characteristic density of $\sim$3000 cm^{-3} and it is mostly O$^+$ ions with smaller amounts of S$^+$ ions present. In the ribbon, $T_e \approx$ 4–5 eV and $T_i \approx$ 10–30 eV. The outermost region is the warm torus, whose center is at Io's orbital distance of 5.9 R_J. It has a scale height of 1 R_J, which makes it the thickest region, and extends from 5.7–8 R_J. The warm torus has a characteristic density of $\sim$2000 cm^{-3} and it is composed of S^{2+} and O$^+$ ions with trace amounts of O^{2+}, S$^+$, and S^{3+} ions. In the warm torus, $T_e \approx$ 5–8 eV and $T_i \approx$ 60 eV.

The scale height, H, is related to plasma composition and temperature [*Thomas*, 1992; *Thomas et al.*, 2004],

$$H = \sqrt{\frac{2k(T_{i,\parallel} + Z_i T_{e,\parallel})}{3M_i\Omega^2}} \tag{1}$$

where k is the Boltzmann constant, $T_{i,\parallel}$ is the ion temperature, Z_i is the atomic number of the ion species, $T_{e,\parallel}$ is the electron temperature, M_i is the mass of the ion species, and Ω is the rotation rate of Jupiter's magnetosphere ($\sim 1.75 \times 10^{-4}$ rad s^{-1}). The $\parallel$

subscripts on T_e and T_i refer to the component of temperature parallel to the magnetic field. Since T_e is much smaller than T_i, the scale height is effectively insensitive to T_e. This scale height defines the extent of the IPT parallel to the magnetic field lines. If a radio occultation can determine the scale height H, then Equation 1 can be used to infer the ion temperature. Doing so requires independent knowledge of the ion composition, which is summarized above.

Previous observations have revealed much about the plasma torus. However, many key science questions still remain concerning the generation, transport, and loss of plasma in the IPT and the magnetosphere of Jupiter. In the context of the IPT itself, outstanding questions include: 1. Over what timescales does the supply of plasma to the IPT vary? 2. How do variations in Io's volcanic activity affect major properties of the IPT? 3. How do major properties of the IPT vary with System III longitude? Multiple radio occultations of the IPT by *Juno* will provide new information for answering these questions. These radio occultations offer unparalleled spatial and temporal coverage of the IPT.

3. Radio occultations

A radio occultation occurs when an object, here the IPT, comes between the transmitter and receiver of a radio signal. On each orbit, *Juno* will pass through the centrifugal equator such that the IPT is between the spacecraft and Earth. This geometry is suitable for radio occultation observations of the torus.

During radio tracking, *Juno* will receive a radio signal from Earth at X-band frequencies (7.3 GHz) and use multipliers to retransmit that signal back to Earth at X-band frequencies (8.4 GHz) and Ka-band frequencies (32.1 GHz) (Table 1) [*Mukai et al.*, 2012]. This method is similar to the method used by Cassini for radio occultations after the failure of its ultrastable oscillator [*Schinder et al.*, 2015] and to the method that will be used by *BepiColombo* for gravity science measurements [*Tommei et al.*, 2015]. Since the downlink frequencies are derived from the same source, the two down-linked radio signals will be transmitted coherently.

The propagation of the radio signal is affected by plasma along its path such that the received frequency contains information about the electron density along the path of the radio signal. As is shown here, the line-of-sight integrated electron density can be derived from comparison of the received frequencies of the two down-linked radio signals.

Neglecting relativistic effects, the received frequency on Earth of the downlinked X-band signal satisfies [*Withers et al.*, 2014]:

$$f_{R,X} = f_{T,X} - \frac{f_{T,X}}{c}\frac{d}{dt}\int dl + \frac{e^2}{8\pi^2 m_e \epsilon_0 c f_{T,X}}\frac{d}{dt}\int N dl - \frac{f_{T,X}\kappa}{c}\frac{d}{dt}\int n dl \qquad (2)$$

where f is frequency, subscripts R and T refer to received and transmitted, respectively, subscript X refers to X-band, c is the speed of light, t is time, l is distance along the ray path, $-e$ is the electron charge, m_e is the electron mass, ϵ_0 is the permittivity of free space, N is the electron density, κ is the mean refractive volume of the neutrals, and n is the number density of neutrals. A similar equation can be written for the received frequency on Earth of the downlinked Ka-band signal:

$$f_{R,Ka} = f_{T,Ka} - \frac{f_{T,Ka}}{c}\frac{d}{dt}\int dl + \frac{e^2}{8\pi^2 m_e \epsilon_0 c f_{T,Ka}}\frac{d}{dt}\int N dl - \frac{f_{T,Ka}\kappa}{c}\frac{d}{dt}\int n dl \qquad (3)$$

The two transmitted frequencies, $f_{T,X}$ and $f_{T,Ka}$, satisfy $f_{T,Ka}/f_{T,X} = f_{D,Ka}/f_{D,X}$, where $f_{D,Ka}/f_{D,X}$ is a fixed ratio of 3344/880 [*Kliore et al.*, 2004]. The subscript D refers to downlinked frequencies. Accordingly, Equation 3 can be multiplied by $f_{D,X}/f_{D,Ka}$ and subtracted from Equation 2 to give:

$$\Delta f = f_{R,X} - f_{R,Ka}\left(\frac{f_{D,X}}{f_{D,Ka}}\right) = \frac{e^2}{8\pi^2 m_e \epsilon_0 c f_{T,X}}\left(1 - \left(\frac{f_{D,X}}{f_{D,Ka}}\right)^2\right)\frac{d}{dt}\int N dl \qquad (4)$$

where Δf is defined as $f_{R,X} - f_{R,Ka}\left(\frac{f_{D,X}}{f_{D,Ka}}\right)$. Terms proportional to the transmitted frequency in Equations 2–3 cancel out in this difference. This eliminates the classical Doppler shift and effects of neutral molecules. The quantity $\int N dl$ is the line-of-sight TEC. If time series of $f_{R,X}$ and $f_{R,Ka}$ are available, Equation 4 can be used to determine the rate of change of the TEC. Given knowledge of the spacecraft trajectory, the time rate of change of the TEC can be converted into the spatial gradient of the TEC. Finally, this can be integrated to give the TEC for each different line of sight.

4. Initial estimate of frequency shifts

We wish to determine how accurately properties of the IPT can be measured by radio occultation experiments. Before developing a sophisticated model of the IPT and sources of noise, we first explore the influence of IPT properties on observable quantities using a simple model.

4.1. Initial model of Io plasma torus

We assume that the electron density N can be represented by a single Gaussian that depends on the distance s' from the center of the torus and that the center of the torus lies in the plane of the centrifugal equator at a distance from Jupiter equal to Io's orbital distance of 5.9 R_J [*Thomas*, 1992; *Thomas et al.*, 2004]. Hence:

$$N\left(s'\right) = N\left(0\right)\exp^{-\frac{s'^2}{H^2}} \tag{5}$$

where H is the scale height and $N\left(0\right)$ is the density at the center of the torus. Typical values for $N\left(0\right)$ and H are 2000 cm^{-3} and 1 R_J, respectively [*Thomas et al.*, 2004]. The critical quantity in Equation 4 is $\int Ndl$, the integral of the electron density along the line of sight. We define TEC as a function of the radio signal's distance of closest approach to the center of the torus s, $TEC\left(s\right)$. This satisfies [*Quémerais et al.*, 2006]:

$$\int Ndl = TEC\left(s\right) = 2\int_s^\infty \frac{N\left(s'\right)s'ds'}{\sqrt{s'^2 - s^2}} \tag{6}$$

where s' is the distance from the center of the IPT to a point on the ray path. With the density N given by Equation 5, $TEC\left(s\right)$ is given by [*Abramowitz and Stegun*, 1972]:

$$TEC\left(s\right) = N(0)\sqrt{\pi}H\exp^{-\frac{s^2}{H^2}} \tag{7}$$

The maximum value of $TEC\left(s\right)$ occurs at $s = 0$, where $TEC = N(0)\sqrt{\pi}H$. For benchmark values $N\left(0\right) = 2000$ cm^{-3} and $H = 1$ R_J, the maximum value of the TEC is 25.5×10^{16} m^{-2}. This can be expressed as 25.5 TECU, where 1 TECU or total electron content unit equals 1×10^{16} m^{-2}.

4.2. Characteristic frequency shifts

Combining Equations 4 and 7, the frequency shift Δf satisfies:

$$\Delta f\left(s\right) = \frac{e^2}{8\pi^2 m_e \epsilon_0 c f_{T,X}}\left(1 - \left(\frac{f_{D,X}}{f_{D,Ka}}\right)^2\right)\frac{d}{dt}\left[N\left(0\right)\sqrt{\pi}H\exp^{-\frac{s^2}{H^2}}\right] \tag{8}$$

Since the only time-variable quantity in Equation 7 is the distance of closest approach s, Equation 8 becomes:

$$\Delta f\left(s\right) = -\frac{e^2}{8\pi^2 m_e \epsilon_0 c f_{T,X}} \left(1 - \left(\frac{f_{D,X}}{f_{D,Ka}}\right)^2\right) \sqrt{\pi} N\left(0\right) \exp^{-\frac{s^2}{H^2}} \left(\frac{2s}{H}\right) \frac{ds}{dt} \tag{9}$$

Here $\frac{ds}{dt}$ is the rate of change of the distance of closest approach s. Note that this refers to the distance of closest approach of the line of sight between the spacecraft and Earth to the center of the IPT. It is therefore affected by the trajectory of the spacecraft and the motion of the IPT, not solely by the trajectory of the spacecraft. For simplicity in this exploratory work, we assume that ds/dt is constant during a radio occultation observation. However, this is a questionable assumption that would need to be revised in the analysis of real observations. First, *Juno*'s speed during a radio occultation observation, which is essentially a periapsis pass, changes appreciably due to the high eccentricity of *Juno*'s orbit. Second, since the IPT is tilted with respect to Jupiter's rotational axis, the center of the IPT moves during a radio occultation observation. At Io's orbital distance, the center of the IPT moves up and down with a velocity of ± 9 kms^{-1} over Jupiter's 9.925 hour rotational period. We assume that $|ds/dt|$ is 20 km s^{-1}, which is a representative value for the spacecraft speed during a periapsis pass (based on the ephemeris tool at www-pw.physics.uiowa.edu/∼jbg/juno.html). This is equivalent to a change in s of one R_J in a time of one hour. We reconsider this issue at the end of Section 4.2.

Equation 9 provides an analytical description of the dependence of the measureable frequency shift Δf on the central density of the torus, $N\left(0\right)$, the torus scale height, H, and ds/dt, which can be intepreted as the projected speed of the spacecraft. The value and location of the maximum value of $|\Delta f|$ can be found by setting the derivative of

Equation 9 with respect to s to zero. The maximum value of $|\Delta f|$, $|\Delta f|_{max}$, occurs at $s^2 = H^2/2$ and satisfies:

$$|\Delta f|_{max} = \frac{e^2}{8\pi^2 m_e \epsilon_0 c f_{T,X}} \left(1 - \left(\frac{f_{D,X}}{f_{D,Ka}}\right)^2\right) \sqrt{\pi} N\left(0\right) e^{-\frac{1}{2}} \sqrt{2} \frac{ds}{dt} \qquad (10)$$

For $N\left(0\right) = 2000$ cm^{-3}, $H = 1\ R_J$, and $|ds/dt| = 20$ km s^{-1}, the maximum value of $|\Delta f|$ is 0.9 mHz. This maximum occurs at $s = 0.7 R_J$.

The top panel of Figure 1 shows how Δf depends on s for several values of $N\left(0\right)$ and fixed $H = 1\ R_J$ and ds/dt = -20 km s^{-1}. We choose a range of values for $N\left(0\right)$ that covers the observed values in the torus. $N\left(0\right)$ varies between 500 cm^{-3} and 2500 cm^{-3} [*Bagenal and Sullivan*, 1981; *Bagenal et al.*, 1997]. The middle panel of Figure 1 shows how Δf depends on s for several values of H and fixed $N\left(0\right) = 2000$ cm^{-3} and ds/dt = -20 km s^{-1}. We choose a range of values for H that covers the observed values in the torus. H varies between 0.5 R$_J$ and 2.5 R$_J$ [*Thomas et al.*, 2004]. The bottom panel in Figure 1 shows how Δf depends on s for several values of $|ds/dt|$ and fixed $N\left(0\right) = 2000$ cm^{-3} and $H = 1\ R_J$. We choose a range of values for $|ds/dt|$ that increases from 20 km s^{-1} to 40 km s^{-1} in increments of 5 km s^{-1}.

Figure 1 illustrates how the observed shift in frequency, Δf, depends on $N\left(0\right)$, H, and ds/dt. Δf is zero at the start of an occultation, when $|s|$ is large. Its magnitude increases monotonically to $\Delta f_{max} = 0.9$ mHz at $s_{crit} = H/\sqrt{2}$, then decreases monotonically through zero at $s = 0$. The behavior of Δf in the second half of the occultation is the same as in the first half, except for a change in sign. The full width at half maximum of the local maximum in Δf is approximately equal to H.

The effects of variations in $N(0)$ and ds/dt are straight-forward, since the frequency shift Δf is proportional to both factors. Spatial and temporal changes in $N(0)$ are likely over the course of the *Juno* mission, since the IPT is intrinsically variable, whereas ds/dt will not vary greatly from orbit to orbit. The effects of variations in H are more complex. As H increases, s_{crit} increases. The width of the local maximum in Δf also increases, but the value of Δf_{max} remains the same.

The timescale, τ, for the radio signal to sweep through the IPT satisfies $|ds/dt|\,\tau = 2H$. With $|ds/dt| = 20$ km s^{-1} and $H = 1R_J$, the timescale τ is approximately 2 hours.

An integration time on the order of 10 seconds provides spatial resolution on the order of $H/100$. For this integration time, it can be assumed that the relative accuracy with which $f_{R,X}$ and $f_{R,Ka}$ can be measured is 3×10^{-14}. This is based on the Allan deviation of the Deep Space Network (DSN) hydrogen masers over a 10 second integration [*Howard et al.*, 1992; *Asmar et al.*, 2005]. With $f_{R,X} = 8.4$ GHz and $f_{R,Ka} = 32.1$ GHz [*Mukai et al.*, 2012], the corresponding uncertainty in a measurement of Δf is 3.8×10^{-4} Hz (Equation 4). This uncertainty in Δf, $\sigma_{\Delta f}$, is 40 percent of the characteristic value of 0.9 mHz discussed above.

The uncertainty on the inferred TEC, σ_{TEC}, follows from propagating the uncertainty in Δf through the integrated version of Equation 4. Assuming a simple numerical integration method leads to:

$$\sigma_{TEC} = \sqrt{\Sigma}\left(\frac{e^2}{8\pi^2 m_e \epsilon_0 c f_{T,X}}\left(1 - \left(\frac{f_{D,X}}{f_{D,Ka}}\right)^2\right)\right)^{-1}\sigma_{\Delta f}\Delta t \qquad (11)$$

where Σ is the number of data points integrated to reach the current measurement and Δt is the integration time for an individual measurement. Since $\Sigma = t/\Delta t$, where t is the time since the start of the observation, we obtain:

$$\left(\frac{\sigma_{TEC}}{1\ \mathrm{TECU}}\right) = 0.5\sqrt{\left(\frac{t}{1\ \mathrm{hr}}\right)\left(\frac{\Delta t}{10\ \mathrm{s}}\right)} \tag{12}$$

For $N(0) = 2000$ cm^{-3}, $H = 1\ R_J$, and $|ds/dt| = 20$ km s^{-1}, $\Delta f_{max} = 0.9$ mHz and $s_{crit} = 0.7\ R_J$. If the integration starts at $s = 4\ R_J$, then t at this local maximum is 3.3 hours from the start of the observation. Henceforth we adopt $\Delta t = 36$ seconds to provide a resolution of 0.01 R_J. This yields $\sigma TEC/\left(1\ \mathrm{TECU}\right) = 0.92\sqrt{t/\left(1\mathrm{hr}\right)}$, which gives σ_{TEC} = 1.68 TECU at the local maximum. In this example, $\sigma_{TEC}/TEC = 7\%$ at the TEC maximum.

Several other potential sources of error must be considered. The effects of noise at the transmitter and receiver on the simulated measurements of frequency shift are accounted for by the stated Allan deviation. The effects of plasma in the rest of Jupiter's environment and the interplanetary medium can be accounted for in the frequency baseline prior to and after the occultation of the IPT [e.g *Thornton and Border*, 2000]. The noise contribution due to the interplanetary medium depends strongly on solar elongation angle. It should be noted that for most of the *Juno* mission the solar elongation angle is relatively large and the associated noise is relatively small [*Woo and Armstrong*, 1979; *Asmar et al.*, 2005]. Plasma in the regions of Jupiter's magnetosphere outside the IPT will also contribute to the measured TEC. At the centrifugal equator, assuming a magnetospheric density 3 cm^{-3} and length of 100 R_J [*Bolton et al.*, 2015], this contribution is about 0.7 TECU, which is small (3%) relative to the peak TEC of the IPT, 25.5 TECU.

Juno's periapsis altitude is approximately 4000 km, which is within the ionosphere [*Bagenal et al.*, 2014]. Hence plasma in Jupiter's ionosphere may contribute to the measured total electron content between the spacecraft and Earth. The ionospheric plasma density at this altitude is approximately 3×10^9 m^{-3} and the ionospheric scale height is on the order of 1000 km [*Eshleman et al.*, 1979b; *Yelle and Miller*, 2004]. This results in a vertical total electron content of 3×10^{15} m^{-2} or 0.3 TECU. The line of sight total electron content will be larger by a geometric factor. This is a potentially significant perturbation to the inferred total electron content of the IPT, especially if passage through the ionosphere occurs as the line of sight to Earth passes through the centrifugal equator. However, the *Juno* Waves instrument is capable of measuring the local plasma density at the spacecraft [*Bagenal et al.*, 2014]. Using its measurements of the vertical structure of the topside ionosphere, the contributions of Jupiter's ionosphere to the inferred total electron content of the IPT can be eliminated.

Since Io orbits Jupiter every 1.7 days, each occultation will measure IPT properties at a different angular separation from Io. A series of occultations over a range of separations from Io will be valuable for assessing how plasma is transported away from Io and into the IPT. It is possible, though unlikely, for an IPT occultation to also probe Io's ionosphere directly. In that event, the line-of-sight total electron content would briefly increase by 0.1 TECU or 1×10^{15} m^{-2}. This follows from a surface ionospheric density of 6×10^3 cm^{-3} and a scale height of 100 km [*Hinson et al.*, 1998].

We previously noted the flaws in the assumption that $\frac{ds}{dt}$ is constant. There are two main consequences if $\frac{ds}{dt}$ is not constant. The first consequence is that it becomes harder to determine the position s associated with a given time in the measured time series of Δf. Yet since the *Juno* trajectory and the location of the centrifugal equator at Io's orbital distance are known, the required mapping from time to position is tractable. The effects of the nodding up and down of the IPT are illustrated in Figure 2. This shows how $\frac{ds}{dt}$ and $s\left(t\right)$ change for different phasings of the motion of the IPT relative to the time of the occultation. This is equivalent to occultations occurring at different System III longitudes. From a fixed vantage point of noon local time in the rotational equator, the IPT moves up and down sinusoidally with a period equal to the planetary rotation period of 9.925 hours, a distance magnitude of 5.89 R_J, and a speed magnitude of 9 km s^{-1}. Given a constant spacecraft speed of 20 km s^{-1}, which is itself a noteworthy simplification, $|ds/dt|$ varies between 10 and 30 km s^{-1}. The variation in ds/dt with time leads to the second consequence, which is that the numerical and graphical results based on Equations 8 and 9 will no longer be perfectly accurate. Furthermore, note that a constant time resolution in the measured received frequencies will no longer correspond to a constant spatial resolution within the IPT.

The only remaining potentially significant source of error is Earth's ionosphere, which is discussed in Section 4.3.

4.3. Initial model of Earth's ionosphere

Plasma densities are much greater in Earth's ionosphere than in Jupiter's magnetosphere or the interplanetary medium. Consequently, plasma in Earth's ionosphere can make a significant contribution to the line-of-sight column density despite the ionosphere's limited vertical extent. If plasma densities in Earth's ionosphere were constant along the line of sight over the duration of the occultation, then they would have no effect on the rate of change of the column density and would not affect the measured frequency shift. This is commonly the case for radio occultation observations of planetary atmospheres and ionospheres, which last for minutes, not hours. However, due to the large size of the IPT and the long duration of an IPT occultation, conditions in Earth's ionosphere along the line of sight from the ground station to the spacecraft may change appreciably over the course of the occultation.

The vertical column density, or vertical total electron content (TEC), of Earth's ionosphere varies with time of day, season, the solar cycle, and other factors [*Maruyama et al.*, 2004; *Bagiya et al.*, 2009]. At nighttime, it can be represented by a constant value of 10 TECU from dusk until dawn. After dawn, it increases smoothly to a peak value of ∼30 TECU at noon, then decreases smoothly to its nighttime value by dusk. This peak TEC of Earth's ionosphere, 30 TECU, is around 1.3 times the peak TEC of the IPT, 25.5 TECU. Moreover, line-of-sight TEC values will be greater than vertical TEC values by a factor of $\sec(\chi)$, where χ is the zenith angle [*Mendillo et al.*, 2004b].

Figure 3 illustrates how line-of-sight TEC through Earth's ionosphere and the IPT varies with time of day for a line-of-sight 30 degrees away from the zenith in which the radio signal passes through the center of the IPT at 9 hours local time. The TEC is the sum of two components. The first component is from Earth's dayside ionosphere. It is given by $A + B\cos\left[2\pi\left(LT - 12\text{hrs}\right)/\left(24\text{hrs}\right)\right]$, where A equals 10 TECU, B equals 20 TECU, and LT is local time. The second component is from the IPT. It is given by $C\exp\left[-\left(LT - 9\text{hrs}\right)^2/\left(1\text{hr}\right)^2\right]$, where C equals 25.5 TECU and 1 hr equals 1 R_J/20 km s^{-1} (Equation 7). We assume benchmark values of $N\left(0\right) = 2000$ cm^{-3} and $H = 1R_J$ for the IPT and a 36 second integration time. Figure 3 also shows representative uncertainties in TEC. For conceptual simplicity, we neglect the variation in uncertainties with time that are defined by Equation 11 and adopt instead a constant uncertainty of 2 TECU. This value comes from the average of Equation 12 over the assumed duration of the occultation. The contributions of Earth's ionosphere to the measured line-of-sight TEC must be subtracted before properties of the IPT can be determined from the observations. We consider two methods for doing so.

First, we do a linear fit to the simulated measurements of TEC at 6–8 and 10–12 hours, then subtract this fit from the simulated measurements of TEC at 7–11 hours. The fit is shown as a red dot-dashed line in Figure 3. The residual TEC, which is shown in the top panel of Figure 4, is the inferred contribution from the IPT. This linear fitting method provides a baseline for the contributions of Earth's ionosphere. As can be seen in the top panel of Figure 4, this method gives torus TEC values that are $\sim$ 1–2 TECU higher than the input torus TEC values from 7–11 hours. Although the corrected simulated measurements of torus TEC values are larger than the input torus TEC values, the difference is less than the measurement uncertainty of 2 TECU. Following Equation 7, we fit the corrected simulated measurements of torus TEC values to a function of the form of $TEC\left(s\right) = TEC\left(0\right) e^{-\frac{s^2}{H^2}}$. The fitted peak TEC value is 27.21±0.06 TECU and the fitted scale height, H, is 1.002±0.002 R_J. This peak TEC is 1.71 TECU larger than the input value of 25.5 TECU. Thus the fitted TEC value is 28 σ away from the input TEC value, but the difference is only 7% of the peak TEC. The fitted scale height is 0.002 R_J larger than the input value of H. The fitted scale height is 1 σ away from the input scale height, but the difference is only 1% of the scale height. The fitted peak TEC value and scale height imply a central density $N\left(0\right)$ of 2127.13 ± 6.33 cm^{-3}. This inferred central density is 127.13 cm^{-3} larger than the input value of 2000 cm^{-3}. The fitted central density value is 20 σ away from the input central density value, but the difference is only 6% of the density. We conclude that this method is reasonable for subtracting the effects of Earth's ionosphere as the errors in the fitted IPT properties are less than 10%. Yet it provides a poor characterization of the uncertainty in the fitted properties.

Second, we subtract modeled direct measurements of the contributions of Earth's ionosphere from the simulated measurements of line-of-sight TEC. The ionospheric contribution is shown as a dashed black line in bottom of Figure 3. Here we assume Earth's ionospheric TEC follows the equation stated above for the dayside ionosphere, but that it is measured imperfectly. GPS receivers at the NASA Deep Space Network (DSN) stations measure the TEC in Earth's ionosphere. The TEC in Earth's ionosphere along the line of sight from the ground station to the spacecraft is routinely reported. We subtract the contributions of Earth's ionosphere, which we assume to be known with an accuracy of 5 TECU [*Thornton and Border*, 2000] from the simulated measurements of TEC, which as before we assume to be known with an accuracy of 2 TECU. The residual TEC, which is shown in the bottom panel of Figure 4, is the inferred contribution from the IPT. With this method, the corrected simulated measurements of TEC values match the input values well, whereas the values obtained with the first method were biased to larger values. However, the measurement uncertainties are larger and thus the formal uncertainties on fitted parameters are also larger. We fit the corrected simulated measurements of TEC values as above. The fitted peak TEC value is 25.5±0.1 TECU, whereas the input value is 25.5 TECU. The difference between fitted and input peak TEC values is $<1\ \sigma$. The fitted scale height, H, is $1.005 \pm 0.007\ R_J$, whereas the input value is 1 R_J. The difference between fitted and input scale heights is $<1\ \sigma$. The fitted peak TEC value and scale height imply a central density, $N(0)$, of 1994.18 ± 14.24 cm^{-3}, whereas the input central density is 2000 cm^{-3}. The difference between fitted and input central densities is $<1\ \sigma$.

We conclude that this method is preferable. It accurately characterizes the fitted parameters. Furthermore the formal uncertainties are consistent with differences between fitted values and input values.

Having established the principle that the IPT can be observed using radio occultations despite the effects of Earth's ionosphere, we neglect Earth's ionosphere in the remainder of this article. More precisely, we assume that the observations occur during the nighttime such that the vertical TEC in Earth's ionosphere is relatively constant. The contribution of Earth's ionosphere to the line-of-sight TEC can be found using either pre- or post-occultation observations, then subtracted from the TEC measurements.

5. Sophisticated model of Io plasma torus

Representing plasma densities in the IPT by a single Gaussian function is convenient and has been useful for testing the effects of changes in plasma and spacecraft parameters and effects of the Earth's ionosphere, but this representation oversimplifies the true density distribution in the IPT.

As discussed in Section 2, the IPT is conventionally divided into three regions: cold torus, ribbon, and warm torus. These three regions have distinct compositions, temperatures, and densities. To better understand temporal and spatial changes in the torus, it is desirable to measure densities in each of its constituent regions. We therefore replace the single Gaussian function of Section 4 with a more sophisticated function that includes contributions for each region.

5.1. Density distribution

We now represent the IPT by four functions, one each for the cold torus and ribbon, and two for the warm torus. In the plane of the centrifugal equator, densities satisfy:

$$N(R < 6.1R_J) = N_1 e^{-\frac{(R-C_1)^2}{(W_1)^2}} + N_2 e^{-\frac{(R-C_2)^2}{(W_2)^2}} + N_3 e^{-\frac{(R-C_3)^2}{(W_3)^2}} \tag{13}$$

$$N(R > 6.1R_J) = N_4 e^{-\frac{(R-C_4)^2}{(W_4)^2}} \tag{14}$$

where R is distance away from the center of Jupiter in the equatorial plane. Equation 13 contains three terms that represent the three regions of the torus: 1. cold torus, 2. ribbon, and 3. warm torus. N_1, N_2, and N_3 correspond to the peak densities of the cold torus, ribbon, and warm torus components, respectively. C_1, C_2, and C_3 are the central locations of the cold torus, ribbon, and warm torus components, respectively. W_1, W_2, and W_3 are the radial widths, in R_J, of the cold torus, ribbon, and warm torus components, respectively. Note that the total density at $R = C_1$, say, is the sum of the three terms. It is not simply N_1.

The warm torus is not well-represented by a single term, which is why Equation 13 only applies at $R < 6.1R_J$. At larger radial distances, the plasma density is given by Equation 14. We label this region as the extended torus. It has peak density N_4, central location C_4, and radial width W_4.

In order to extend this model beyond the plane of the centrifugal equator, we multiply each term in Equations 13–14 by factor of $e^{-\frac{r^2}{H^2}}$ where r is distance away from the plane of the centrifugal equator. Therefore $N\left(R, r\right)$ satisfies:

$$N(R < 6.1R_J, r) = N_1 e^{-\frac{(R-C_1)^2}{(W_1)^2}} e^{-\frac{r^2}{H_1^2}} + N_2 e^{-\frac{(R-C_2)^2}{(W_2)^2}} e^{-\frac{r^2}{H_2^2}} + N_3 e^{-\frac{(R-C_3)^2}{(W_3)^2}} e^{-\frac{r^2}{H_3^2}} \qquad (15)$$

$$N(R > 6.1R_J, r) = N_4 e^{-\frac{(R-C_4)^2}{(W_4)^2}} e^{-\frac{r^2}{H_3^2}} \qquad (16)$$

H_1, H_2, H_3, and H_3 are the scale heights of the cold torus, ribbon, warm torus, and extended torus components, respectively. Note that the warm torus and extended torus have the same scale height, H_3.

The functional form represented by Equations 13–14 was adopted in order to reproduce the radial density distribution for the centrifugal equator shown in Figure 6 of *Bagenal and Sullivan* [1981]. Numerical values of the corresponding model parameters, which were determined by a fit to the data shown in that figure, are given in Table 2. Numerical values of the model scale heights, which were determined from Figure 12 in *Bagenal and Sullivan* [1981], are given in Table 2. A schematic of the model IPT and the occultation geometry is shown in Figure 5. The modeled electron densities are shown in Figure 6. Figure 6 also demonstrates that this model provides a good representation of the density observations in the centrifugal equator reported in Figure 6 of *Bagenal and Sullivan* [1981].

5.2. Simulated *Juno* radio occultation

To simulate a radio occultation through this representation of the IPT, we assume that the line of sight from *Juno* to Earth is parallel to the centrifugal equator. We assume that the spacecraft velocity in the direction normal to the centrifugal equatorial plane is -20 km s^{-1}, assume that nodding motion of the IPT due to Jupiter's rapid rotation can be neglected, and use an integration time of 36 seconds, which corresponds to a sampling rate of 0.03 Hz. Figure 7 shows the TEC and its rate of change. Figure 8 shows the corresponding noise-free frequency shift Δf (Equation 4) and the noisy frequency shift Δf. Following Section 4, for relative measurement uncertainties of 3×10^{-14} on $f_{R,X}$ and $f_{R,Ka}$, the uncertainty on a single measurement of Δf is 3.8×10^{-4} Hz. The uncertainties are added to the frequency shifts pulling from a random normal distribution with mean zero and standard deviation of 3.8×10^{-4} Hz.

The simulated measurements of TEC were found by integration of the frequency shift Δf using Equation 4. Uncertainties in the TEC were derived from the uncertainty in Δf by repeated application of the standard error propagation formula. The top panel of Figure 9 shows the simulated measurements of TEC, corresponding uncertainties, and the input TEC. The bottom panel shows the difference between simulated measurements of TEC and the input TEC.

It is noticeable that the relative uncertainties on the TEC (Figure 9) are much less than those on the frequency shift (Figure 8) from which TEC was derived. This is an example of integration reducing the importance of random noise.

5.3. Fitted Io plasma torus parameters and their accuracy

Section 4 explored the accuracy with which a central density and scale height could be fit to simulated TEC observations. However, this used a simple single Gaussian model of the IPT. Here we fit the simulated TEC measurements from Section 5 to a model that includes multiple Gaussian contributions in order to determine the accuracy with which the central density and scale height of the cold torus, ribbon, and warm torus can be measured.

For clarity in this initial exploration of this topic, we assume that the radio occultation is observed at nighttime. During the night, the TEC of Earth's ionosphere is relatively constant. A constant TEC will have no effect on the measured frequency shift (Equation 4). Consequently we neglect the effects of Earth's ionosphere and fit the simulated TEC observations shown in Figure 9.

Since the line-of-sight between the spacecraft and Earth is assumed to be parallel to the plane of the centrifugal equator, each radio ray path has a constant value of r. The model TEC along the ray path with closest approach distance r is derived in Appendix A. It satisfies:

$$TEC\,(r) = \sqrt{\pi} N_1 W_1 e^{-\frac{r^2}{H_1^2}} + \sqrt{\pi} N_2 W_2 e^{-\frac{r^2}{H_2^2}} + \tag{17}$$
$$\frac{\sqrt{\pi}}{2}\left[N_3 W_3 \left(1 + \frac{(6.1R_J - C_3)}{W_3}\right) + N_4 W_4 \left(1 - \frac{(6.1R_J - C_4)}{W_4}\right)\right] e^{-\frac{r^2}{H_3^2}}$$

Due to their different scale heights, the three regions of the IPT each make distinct and potentially separable contributions to the overall TEC. We therefore fit the simulated TEC observations to a function of the form:

$$TEC(r) = Ae^{-\frac{r^2}{B^2}} + Ce^{-\frac{r^2}{D^2}} + Ee^{-\frac{r^2}{F^2}} \tag{18}$$

The parameters A, C, and E corresponds to the peak or equatorial TEC for each of the regions and the parameters B, D, and F correspond to the scale heights of the cold torus (H_1), ribbon (H_2), and warm torus (H_3), respectively.

We fit this equation to the simulated TEC observations shown in Figure 10 using a Markov Chain Monte Carlo (MCMC) method. This is implemented using the Python module emcee, which is an open source MCMC ensemble sampler developed by *Foreman-Mackey et al.* [2013].

Figure 10 shows the simulated measurements and fitted TEC, as well as the residuals between the simulated measurements and the fit. Table 3 shows the best fit parameters for each region compared to the input values. Two of the three fitted peak electron content values are within 1 σ of their input values, and the other is within 2 σ, which demonstrates that they are reliable. All three fitted scale heights are within 10% and 1 σ of their input values.

6. Discussion

The preceding sections showed how radio signals from the *Juno* spacecraft could be used to measure TEC profiles for the IPT, that uncertainties on measured TEC are relatively small, and that a fit to the measured TEC can determine the scale height and peak TEC for each of the three regions of IPT (cold torus, ribbon, and warm torus).

Ion temperatures can be derived from scale heights via Equation 1. We assume that S^+ dominate in the cold torus, O^+ dominates in the ribbon, and S^{2+} and O^+ dominates in the warm torus such that the mean molecular mass is 24 daltons [*Thomas et al.*, 2004]. We use the best fit parameters and uncertainties reported in Table 3 to find ion temperatures of $0.957^{+0.173}_{-0.173}$ eV for the cold torus, $16.7^{+1.58}_{-2.47}$ eV for the ribbon and $56.9^{+6.05}_{-5.51}$ eV for the warm torus. For reference, the ion temperatures reported by *Thomas et al.* [2004] and discussed in Section 2 are 1–4 eV for the cold torus, 10–30 eV for the ribbon, and ≈60 eV for the warm torus. Hence the fitted ion temperatures are reasonable for the cold torus, ribbon, and the warm torus.

The peak or equatorial TEC of each region can be determined by fitting Equation 18 to the observed $TEC\,(r)$. For the cold torus and ribbon, peak TEC equals $\sqrt{\pi}N_iW_i$, where N_i is the maximum density in region i and W_i is the width of region i. For the warm torus and its extension beyond 6.1 R_J, peak TEC is more complicated (Equation 17). Nevertheless, it can be considered as the product of a maximum density and an effective width. If the width of a region is known from independent measurements or models of the IPT, then the maximum density for that region can be found from the observed peak TEC. As noted by *Bird et al.* [1992], the electron density in a region cannot be accurately determined from an observed peak TEC without independent knowledge of the width and central peak location of that region.

The analysis described in this article assumes that the line of sight from *Juno* to Earth is parallel to the plane of the centrifugal equator. If that is not the case, then the measured TEC values would correspond to cuts through the torus at the angle between the line of sight and the centrifugal equator. This is equivalent to the IPT being tilted. A tilted torus can be accounted for by a suitable adjustment of the assumed Gaussian profile, as in the model by *Divine and Garrett* [1983].

7. Conclusions

When the line of sight between *Juno* and Earth passes through the Io plasma torus, which occurs once per orbit, radio signals from the *Juno* spacecraft can be used to measure total electron content profiles for the Io plasma torus. We develop a model of densities in the Io plasma torus using values measured by the *Voyager 1* spacecraft and reported in *Bagenal and Sullivan* [1981], then use it to simulate a dual-frequency radio occultation performed using the telecommunication subsystem on the *Juno* spacecraft. Using the modeled densities we calculate the total electron content by integrating along a line of sight parallel to the torus equator. From the total electron content we are able to derive the frequency shift that would be measured by the Deep Space Network receiving stations.

This is then used with error introduced equal to the Allan deviation corresponding to an integration time on the order of 10s to determine a simulated profile of the measured total electron content.

Uncertainties on the measured total electron content are relatively small ($\sim$10%). A Markov chain Monte Carlo fit to the measured total electron content can determine the scale height and peak total electron content for each of the three regions of Io plasma torus (cold torus, ribbon, and warm torus). The ion temperature in each region can be determined from the scale height assuming independent knowledge of the ion composition. The peak total electron content in each region is proportional to the product of the peak local electron density and the region's width in the equatorial plane. However, without independent knowledge of one of these two factors, the other cannot be determined directly. Numerical modeling of the Io plasma torus may be useful in narrowing the range of possible peak local electron densities and widths.

To date, only two radio occultations of the Io plasma torus have been performed, *Voyager 1* [*Eshleman et al.*, 1979a] and *Ulysses* [*Bird et al.*, 1992]. *Juno* has the potential to perform over 20 occultations. This series of occultations would provide a rich picture of the structure of the Io plasma torus and its temporal and spatial variability.

The *Juno* mission presents an unparalleled opportunity to study the flow of material from the volcanoes of Io to the auroral regions of Jupiter with simultaneous observations of all stages in this system. Ground-based infrared observations of Io can be used to monitor the moon's volcanic activity [*de Kleer et al.*, 2014]. Ground-based sodium cloud observations can be used to monitor the transport of material from Io's atmosphere into the neutral clouds, since sodium can be considered as a tracer for sulfur and oxygen

[*Wilson et al.*, 2002; *Mendillo et al.*, 2004a; *Thomas et al.*, 2004]. Radio occultations can be used to monitor the ionization of neutral species and the distribution of plasma within the Io plasma torus [*Eshleman et al.*, 1979a; *Bird et al.*, 1992]. *Juno*'s suite of plasma instruments will monitor plasma densities in the acceleration regions near Jupiter's poles [*Bagenal et al.*, 2014]. Together, the measurements already planned by the *Juno* mission, the potential radio occultations of the Io plasma torus, and Earth-based observations of the Jupiter system will reveal the complete life-cycle of plasma in Jupiter's magnetosphere.

Appendix A: Total electron content

Since the line-of-sight between the spacecraft and Earth is assumed to be parallel to the plane of the centrifugal equator, each radio ray path has a constant value of r. The total electron content along the ray path with closest approach distance r, $TEC\left(r\right)$, satisfies:

$$\begin{aligned} TEC\left(r\right) = {} & N_1 W_1 \frac{\sqrt{\pi}}{2}\left(erf\left[\frac{C_1}{W_1}\right] + erf\left[\frac{(6.1R_J - C_1)}{W_1}\right]\right) e^{-\frac{r^2}{H_1^2}} + \\ & N_2 W_2 \frac{\sqrt{\pi}}{2}\left(erf\left[\frac{C_2}{W_2}\right] + erf\left[\frac{(6.1R_J - C_2)}{W_2}\right]\right) e^{-\frac{r^2}{H_2^2}} + \\ & N_3 W_3 \frac{\sqrt{\pi}}{2}\left(erf\left[\frac{C_3}{W_3}\right] + erf\left[\frac{(6.1R_J - C_3)}{W_3}\right]\right) e^{-\frac{r^2}{H_3^2}} + \\ & N_4 W_4 \frac{\sqrt{\pi}}{2}\left(erf\left[\frac{C_4}{W_4}\right] - erf\left[\frac{(6.1R_J - C_4)}{W_4}\right]\right) e^{-\frac{r^2}{H_3^2}} \end{aligned} \tag{A1}$$

where $erf\left(x\right)$ is the error function. For all plausible conditions, C_1/W_1, C_2/W_2, C_3/W_3, and C_4/W_4 are much greater than one. Since $erf\left(x \gg 1\right) = 1$, Equation A1 becomes:

$$\begin{aligned} TEC\left(r\right) = {} & N_1 W_1 \frac{\sqrt{\pi}}{2}\left(1 + erf\left[\frac{(6.1R_J - C_1)}{W_1}\right]\right) e^{-\frac{r^2}{H_1^2}} + \\ & N_2 W_2 \frac{\sqrt{\pi}}{2}\left(1 + erf\left[\frac{(6.1R_J - C_2)}{W_2}\right]\right) e^{-\frac{r^2}{H_2^2}} + \end{aligned} \tag{A2}$$

$$N_3 W_3 \frac{\sqrt{\pi}}{2}\left(1 + erf\left[\frac{(6.1R_J - C_3)}{W_3}\right]\right) e^{-\frac{r^2}{H_3^2}} +$$
$$N_4 W_4 \frac{\sqrt{\pi}}{2}\left(1 - erf\left[\frac{(6.1R_J - C_4)}{W_4}\right]\right) e^{-\frac{r^2}{H_3^2}}$$

Furthermore, $(6.1R_J - C_1)/W_1$ and $(6.1R_J - C_2)/W_2$ can also be expected to be greater than one, which gives:

$$\begin{aligned} TEC(r) = \sqrt{\pi} N_1 W_1 e^{-\frac{r^2}{H_1^2}} &+ \\ \sqrt{\pi} N_2 W_2 e^{-\frac{r^2}{H_2^2}} &+ \\ N_3 W_3 \frac{\sqrt{\pi}}{2}\left(1 + erf\left[\frac{(6.1R_J - C_3)}{W_3}\right]\right) e^{-\frac{r^2}{H_3^2}} &+ \\ N_4 W_4 \frac{\sqrt{\pi}}{2}\left(1 - erf\left[\frac{(6.1R_J - C_4)}{W_4}\right]\right) e^{-\frac{r^2}{H_3^2}} & \end{aligned} \tag{A3}$$

In our model, $(6.1R_J - C_3)/W_3 = 0.66$ and $(6.1R_J - C_4)/W_4 = 0.30$. The error function $erf(x)$ increases from 0 at $x = 0$ to 1 at $x \gg 1$. It can be approximated as $erf(x) = x$ for $x < 1$ and $erf(x) = 1$ for $x > 1$. The error in this approximation is less than 0.15 for all x. We therefore assume that $(6.1R_J - C_3)/W_3 < 1$ and $(6.1R_J - C_4)/W_4 < 1$, which leads to:

$$\begin{aligned} TEC(r) = \sqrt{\pi} N_1 W_1 e^{-\frac{r^2}{H_1^2}} + \sqrt{\pi} N_2 W_2 e^{-\frac{r^2}{H_2^2}} &+ \\ \frac{\sqrt{\pi}}{2}\left[N_3 W_3 \left(1 + \frac{(6.1R_J - C_3)}{W_3}\right) + N_4 W_4 \left(1 - \frac{(6.1R_J - C_4)}{W_4}\right)\right] e^{-\frac{r^2}{H_3^2}} & \end{aligned} \tag{A4}$$

Expanding the term in square brackets further does not provide additional insight.

Acknowledgments. PHP was supported, in part, by the Massachusetts Space Grant Consortium (MASGC). PHP would also like to thank Mark Veyette and Paul Dalba for useful discussions. We would like to thank the two anonymous reviewers for their suggestions. No data were used in this article.

References

Abramowitz, M., and I. A. Stegun (1972), *Handbook of Mathematical Functions*, 295-300 pp., Dover.

Asmar, S. W., J. W. Armstrong, L. Iess, and P. Tortora (2005), Spacecraft Doppler tracking: Noise budget and accuracy achievable in precision radio science observations, *Radio Science*, *40*, RS2001, doi:10.1029/2004RS003101.

Bagenal, F. (1994), Empirical model of the Io plasma torus: Voyager measurements, *J. Geophys. Res.*, *99*, 11,043–11,062, doi:10.1029/93JA02908.

Bagenal, F., and P. A. Delamere (2011), Flow of mass and energy in the magnetospheres of Jupiter and Saturn, *J. Geophys. Res.*, *116*, A05209, doi:10.1029/2010JA016294.

Bagenal, F., and J. D. Sullivan (1981), Direct plasma measurements in the Io torus and inner magnetosphere of Jupiter, *J. Geophys. Res.*, *86*, 8447–8466, doi:10.1029/JA086iA10p08447.

Bagenal, F., F. J. Crary, A. I. F. Stewart, N. M. Schneider, D. A. Gurnett, W. S. Kurth, L. A. Frank, and W. R. Paterson (1997), Galileo measurements of plasma density in the Io torus, *Geophys. Res. Lett.*, *24*, 2119, doi:10.1029/97GL01254.

Bagenal, F., A. Adriani, F. Allegrini, S. J. Bolton, B. Bonfond, E. J. Bunce, J. E. P. Connerney, S. W. H. Cowley, R. W. Ebert, G. R. Gladstone, C. J. Hansen, W. S. Kurth, S. M. Levin, B. H. Mauk, D. J. McComas, C. P. Paranicas, D. Santos-Costa, R. M. Thorne, P. Valek, J. H. Waite, and P. Zarka (2014), Magnetospheric Science

Objectives of the Juno Mission, *Space Sci. Rev.*, doi:10.1007/s11214-014-0036-8.

Bagiya, M. S., H. P. Joshi, K. N. Iyer, M. Aggarwal, S. Ravindran, and B. M. Pathan (2009), TEC variations during low solar activity period (2005-2007) near the Equatorial Ionospheric Anomaly Crest region in India, *Annales Geophysicae*, *27*, 1047–1057, doi:10.5194/angeo-27-1047-2009.

Bird, M. K., S. W. Asmar, J. P. Brenkle, P. Edenhofer, O. Funke, M. Paetzold, and H. Volland (1992), Ulysses radio occultation observations of the Io plasma torus during the Jupiter encounter, *Science*, *257*, 1531–1535, doi:10.1126/science.257.5076.1531.

Bird, M. K., S. W. Asmar, P. Edenhofer, O. Funke, M. Pätzold, and H. Volland (1993), The structure of Jupiter's Io plasma torus inferred from Ulysses radio occultation observations, *Planet. Space Sci.*, *41*, 999–1010, doi:10.1016/0032-0633(93)90104-A.

Bolton, S. J., F. Bagenal, M. Blanc, T. Cassidy, E. Chané, C. Jackman, X. Jia, A. Kotova, N. Krupp, A. Milillo, C. Plainaki, H. T. Smith, and H. Waite (2015), Jupiter's Magnetosphere: Plasma Sources and Transport, *Space Sci. Rev.*, *192*, 209–236, doi:10.1007/s11214-015-0184-5.

Bonfond, B., D. Grodent, J.-C. Gérard, T. Stallard, J. T. Clarke, M. Yoneda, A. Radioti, and J. Gustin (2012), Auroral evidence of Io's control over the magnetosphere of Jupiter, *Geophys. Res. Lett*, *39*, L01105, doi:10.1029/2011GL050253.

Brown, M. E. (1995), Periodicities in the Io plasma torus, *J. Geophys. Res.*, *100*, 21,683–21,696, doi:10.1029/95JA01988.

Brown, R. A. (1976), A model of Jupiter's sulfur nebula, *Astrophys. J. Lett*, *206*, L179–L183, doi:10.1086/182162.

Campbell, J. K., and S. P. Synnott (1985), Gravity field of the Jovian system from Pioneer and Voyager tracking data, *Astron. J.*, *90*, 364–372, doi:10.1086/113741.

Carlson, R. W., and D. L. Judge (1975), Pioneer 10 ultraviolet photometer observations of the Jovian hydrogen torus — The angular distribution, *Icarus*, *24*, 395–399, doi:10.1016/0019-1035(75)90055-X.

Connerney, J., S. Bolton, and S. Levin (2016), The Juno New Frontier Mission: Inside and Out, in *EGU General Assembly Conference Abstracts*, *EGU General Assembly Conference Abstracts*, vol. 18, p. 18023.

de Kleer, K., I. de Pater, A. G. Davies, and M. Ádámkovics (2014), Near-infrared monitoring of Io and detection of a violent outburst on 29 August 2013, *Icarus*, *242*, 352–364, doi:10.1016/j.icarus.2014.06.006.

Dessler, A. J. (2002), *Physics of the Jovian Magnetosphere*, pp. 438–441, Cambridge, UK: Cambridge University Press.

Divine, N., and H. B. Garrett (1983), Charged particle distributions in Jupiter's magnetosphere, *J. Geophys. Res.*, *88*, 6889–6903, doi:10.1029/JA088iA09p06889.

Eshleman, V. R., G. L. Tyler, G. E. Wood, G. F. Lindal, J. D. Anderson, G. S. Levy, and T. A. Croft (1979a), Radio science with Voyager at Jupiter — Initial Voyager 2 results and a Voyager 1 measure of the Io torus, *Science*, *206*, 959–962, doi:10.1126/science.206.4421.959.

Eshleman, V. R., G. L. Tyler, G. E. Wood, G. F. Lindal, J. D. Anderson, G. S. Levy, and T. A. Croft (1979b), Radio science with Voyager 1 at Jupiter - Preliminary profiles of the atmosphere and ionosphere, *Science*, *204*, 976–978, doi:10.1126/science.204.4396.976.

Foreman-Mackey, D., D. W. Hogg, D. Lang, and J. Goodman (2013), emcee: The MCMC Hammer, *Publ. A. S. P.*, *125*, 306–312, doi:10.1086/670067.

Hill, T. W., A. J. Dessler, and F. C. Michel (1974), Configuration of the Jovian magnetosphere, *Geophys. Res. Lett*, *1*, 3–6, doi:10.1029/GL001i001p00003.

Hill, T. W., A. J. Dessler, and L. J. Maher (1981), Corotating magnetospheric convection, *J. Geophys. Res.*, *86*, 9020–9028, doi:10.1029/JA086iA11p09020.

Hinson, D. P., A. J. Kliore, F. M. Flasar, J. D. Twicken, P. J. Schinder, and R. G. Herrera (1998), Galileo radio occultation measurements of Io's ionosphere and plasma wake, *J. Geophys. Res.*, *103*, 29,343–29,358, doi:10.1029/98JA02659.

Howard, H. T., V. R. Eshleman, D. P. Hinson, A. J. Kliore, G. F. Lindal, R. Woo, M. K. Bird, H. Volland, P. Edenhoffer, and M. Paetzold (1992), Galileo radio science investigations, *Space Sci. Rev.*, *60*, 565–590, doi:10.1007/BF00216868.

Judge, D. L., and R. W. Carlson (1974), Pioneer 10 Observations of the Ultraviolet Glow in the Vicinity of Jupiter, *Science*, *183*, 317–318, doi:10.1126/science.183.4122.317.

Khurana, K. K., M. G. Kivelson, V. M. Vasyliunas, N. Krupp, J. Woch, A. Lagg, B. H. Mauk, and W. S. Kurth (2004), *The configuration of Jupiter's magnetosphere*, pp. 593–616, Cambridge, UK: Cambridge University Press.

Kliore, A. J., J. D. Anderson, J. W. Armstrong, S. W. Asmar, C. L. Hamilton, N. J. Rappaport, H. D. Wahlquist, R. Ambrosini, F. M. Flasar, R. G. French, L. Iess, E. A. Marouf, and A. F. Nagy (2004), Cassini Radio Science, *Geophys. Res. Lett*, *115*, 1–70, doi:10.1007/s11214-004-1436-y.

Kupo, I., Y. Mekler, and A. Eviatar (1976), Detection of ionized sulfur in the Jovian magnetosphere, *Astrophys. J. Lett*, *205*, L51–L53, doi:10.1086/182088.

Levy, G. S., D. W. Green, H. N. Royden, G. E. Wood, and G. L. Tyler (1981), Dispersive Doppler measurement of the electron content of the torus of Io, *J. Geophys. Res.*, *86*, 8467–8470, doi:10.1029/JA086iA10p08467.

Maruyama, T., G. Ma, and M. Nakamura (2004), Signature of TEC storm on 6 November 2001 derived from dense GPS receiver network and ionosonde chain over Japan, *J. Geophys. Res.*, *109*(A18), A10302, doi:10.1029/2004JA010451.

Mendillo, M., J. Wilson, J. Spencer, and J. Stansberry (2004a), Io's volcanic control of Jupiter's extended neutral clouds, *Icarus*, *170*, 430–442, doi: 10.1016/j.icarus.2004.03.009.

Mendillo, M., X. Pi, S. Smith, C. Martinis, J. Wilson, and D. Hinson (2004b), Ionospheric effects upon a satellite navigation system at Mars, *Radio Science*, *39*, RS2028, doi: 10.1029/2003RS002933.

Mukai, R., D. Hansen, A. Mittskus, J. Taylor, and M. Danos (2012), Juno Telecommunications, in *Design and Performance Summary Series*, 16, http://descanso.jpl.nasa.gov/DPSummary/summary.html.

Nozawa, H., H. Misawa, S. Takahashi, A. Morioka, S. Okano, and R. Sood (2004), Long-term variability of [SII] emissions from the Io plasma torus between 1997 and 2000, *J. Geophys. Res.*, *109*, A07209, doi:10.1029/2003JA010241.

Nozawa, H., H. Misawa, S. Takahashi, A. Morioka, S. Okano, and R. Sood (2005), Relationship between the Jovian magnetospheric plasma density and Io torus emission, *Geophys. Res. Lett.*, *32*, L11101, doi:10.1029/2005GL022759.

Nozawa, H., H. Misawa, M. Kagitani, F. Tsuchiya, S. Takahashi, A. Morioka, T. Kimura, S. Okano, H. Yamamoto, and R. Sood (2006), Implication for the solar wind effect on the Io plasma torus, *Geophys. Res. Lett.*, *33*, L16103, doi:10.1029/2005GL025623.

Payan, A. P., A. Rajendar, C. S. Paty, and F. Crary (2014), Effect of plasma torus density variations on the morphology and brightness of the Io footprint, *J. Geophys. Res.*, *119*, 3641–3649, doi:10.1002/2013JA019299.

Pilcher, C. B., and J. S. Morgan (1979), Detection of singly ionized oxygen around Jupiter, *Science*, *205*, 297, doi:10.1126/science.205.4403.297.

Quémerais, E., J.-L. Bertaux, O. Korablev, E. Dimarellis, C. Cot, B. R. Sandel, and D. Fussen (2006), Stellar occultations observed by SPICAM on Mars Express, *J. Geophys. Res.*, *111*, E09S04, doi:10.1029/2005JE002604.

Schinder, P. J., F. M. Flasar, E. A. Marouf, R. G. French, A. Anabtawi, E. Barbinis, and A. J. Kliore (2015), A numerical technique for two-way radio occultations by oblate axisymmetric atmospheres with zonal winds, *Radio Science*, *50*, 712–727, doi: 10.1002/2015RS005690.

Schneider, N. M., and J. T. Trauger (1995), The Structure of the Io Torus, *Astrophys. J.*, *450*, 450, doi:10.1086/176155.

Smyth, W. H. (1992), Neutral cloud distribution in the Jovian system, *Advances in Space Research*, *12*, 337–346, doi:10.1016/0273-1177(92)90408-P.

Smyth, W. H., and M. R. Combi (1988), A general model for Io's neutral gas clouds. II - Application to the sodium cloud, *Astrophys. J.*, *328*, 888–918, doi:10.1086/166346.

Steffl, A. J., A. I. F. Stewart, and F. Bagenal (2004a), Cassini UVIS observations of the Io plasma torus. I. Initial results, *Icarus*, *172*, 78–90, doi:10.1016/j.icarus.2003.12.027.

Steffl, A. J., F. Bagenal, and A. I. F. Stewart (2004b), Cassini UVIS observations of the Io plasma torus. II. Radial variations, *Icarus*, *172*, 91–103, doi: 10.1016/j.icarus.2004.04.016.

Thomas, N. (1992), Optical observations of Io's neutral clouds and plasma torus, *Surveys* *in Geophysics*, *13*, 91–164, doi:10.1007/BF01903525.

Thomas, N., F. Bagenal, T. W. Hill, and J. K. Wilson (2004), The Io neutral clouds and plasma torus, in *Jupiter: The Planet, Satellites and Magnetosphere*, edited by F. Bagenal, T. E. Dowling, and W. B. McKinnon, pp. 561–591, Cambridge, UK: Cambridge University Press.

Thornton, C., and J. Border (2000), Radiometric Tracking Techniques for Deep-Space Navigation, in *DEEP-SPACE COMMUNICATIONS AND NAVIGATION SERIES*, vol. 1, edited by J. Yuen, Jet Propulsion Laboratory, California Institute of Technology. Available at http://descanso.jpl.nasa.gov/monograph/mono.html.

Tommei, G., L. Dimare, D. Serra, and A. Milani (2015), On the Juno radio science experiment: models, algorithms and sensitivity analysis, *Mon. Not. R. Astron. Soc.*, *446*, 3089–3099, doi:10.1093/mnras/stu2328.

Wilson, J. K., M. Mendillo, J. Baumgardner, N. M. Schneider, J. T. Trauger, and B. Flynn (2002), The Dual Sources of Io's Sodium Clouds, *Icarus*, *157*, 476–489, doi:10.1006/icar.2002.6821.

Withers, P., L. Moore, K. Cahoy, and I. Beerer (2014), How to process radio occultation data: 1. From time series of frequency residuals to vertical profiles of atmospheric and ionospheric properties, *Planet. Space Sci.*, *101*, 77–88, doi:10.1016/j.pss.2014.06.011.

Woo, R., and J. W. Armstrong (1979), Spacecraft radio scattering observations of the power spectrum of electron density fluctuations in the solar wind, *J. Geophys. Res.*, *84*, 7288–7296, doi:10.1029/JA084iA12p07288.

Yelle, R. V., and S. Miller (2004), Jupiter's thermosphere and ionosphere, in *Jupiter. The Planet, Satellites and Magnetosphere*, edited by F. Bagenal, T. E. Dowling, and W. B.

McKinnon, pp. 185–218, Cambridge, UK: Cambridge University Press.

Yoneda, M., M. Kagitani, and S. Okano (2009), Short-term variability of Jupiter's extended sodium nebula, *Icarus*, *204*, 589–596, doi:10.1016/j.icarus.2009.07.023.

Yoneda, M., H. Nozawa, H. Misawa, M. Kagitani, and S. Okano (2010), Jupiter's magnetospheric change by Io's volcanoes, *Geophys. Res. Lett.*, *37*, L11202, doi:10.1029/2010GL043656.

Yoneda, M., F. Tsuchiya, H. Misawa, B. Bonfond, C. Tao, M. Kagitani, and S. Okano (2013), Io's volcanism controls Jupiter's radio emissions, *Geophys. Res. Lett.*, *40*, 671–675, doi:10.1002/grl.50095.

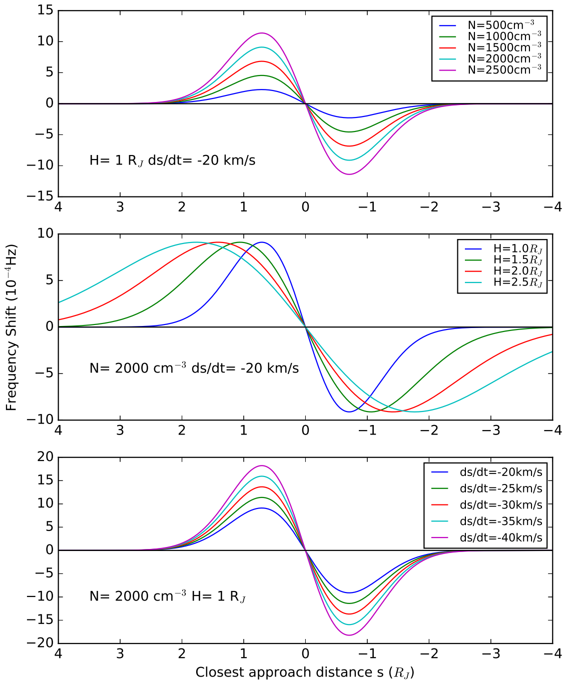

Figure 1. (top) Dependence of frequency shift on closest approach distance s for initial model of torus. Different lines represent different values for $N(0)$. (middle) Dependence of frequency shift on closest approach distance s for initial model of torus. Different lines represent different values for H. (bottom) Dependence of frequency shift on closest approach distance s for initial model of torus. Different lines represent different values for ds/dt. The quantities that are held fixed in each panel are shown in the bottom left corners.

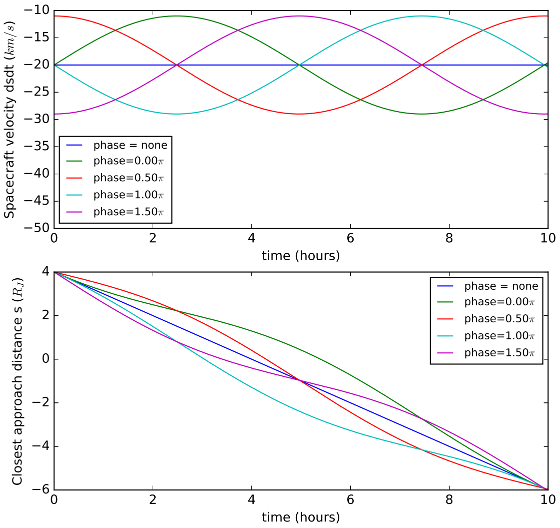

Figure 2. (top) Dependence of ds/dt on time when the spacecraft is moving at a constant speed of 20 km s^{-1} and the Io plasma torus is moving with a sinusoidally-varying speed that has a period of 9.925 hours and an amplitude of 9 km s^{-1}. Different lines show different phases for the motion of the Io plasma torus. The horizontal line that corresponds to a fixed Io plasma torus is for reference. (bottom) Corresponding dependence of distance of closest approach, s, on time. Line colors are as in the top panel. The diagonal line that corresponds to a fixed Io plasma torus and constant ds/dt is for reference.

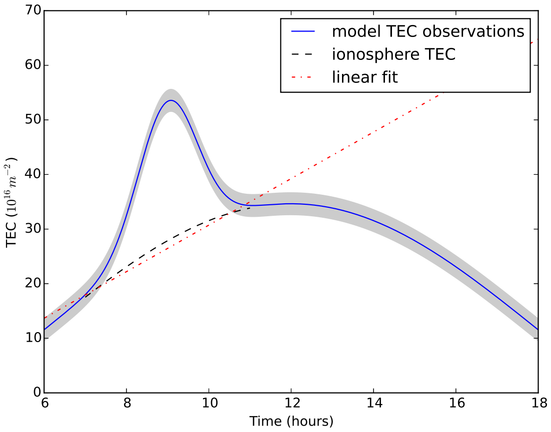

Figure 3. Modeled line of sight total electron content between spacecraft and ground-based antenna during an occultation of the Io plasma torus as a function of local time at the ground-based antenna. The contribution of the Io plasma torus can be seen above the background contribution of Earth's ionosphere between 8 and 10 hours local time. The gray shaded region indicates the uncertainty on the measured total electron content. The black dashed line represents the modeled ionospheric TEC. The red dot-dashed line represents the linear fit to the background.

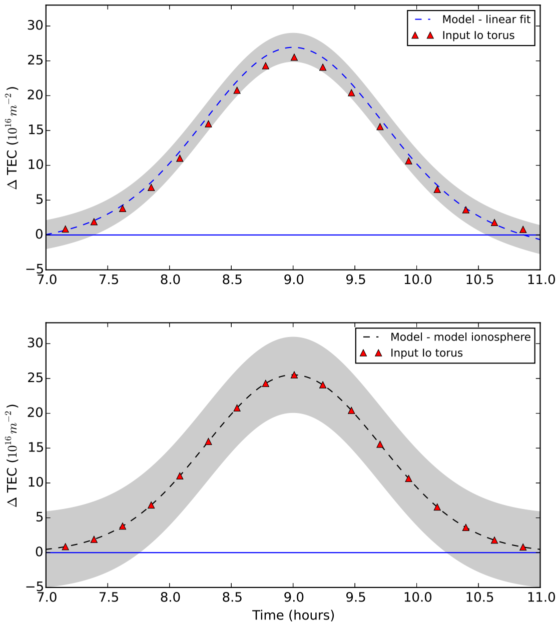

Figure 4. (top) The dashed line shows the difference between the total electron content measurements from Figure 3 and a linear fit to background values either side of the occultation. (bottom) The dashed line shows the difference between the total electron content measurements from Figure 3 and independent measurements of the total electron content in Earth's ionosphere. The differences shown in these panels are the inferred total electron contents of the Io plasma torus. The gray shaded regions show the uncertainties on the inferred total electron content of the Io plasma torus and the red triangles show the input total electron content of the Io plasma torus.

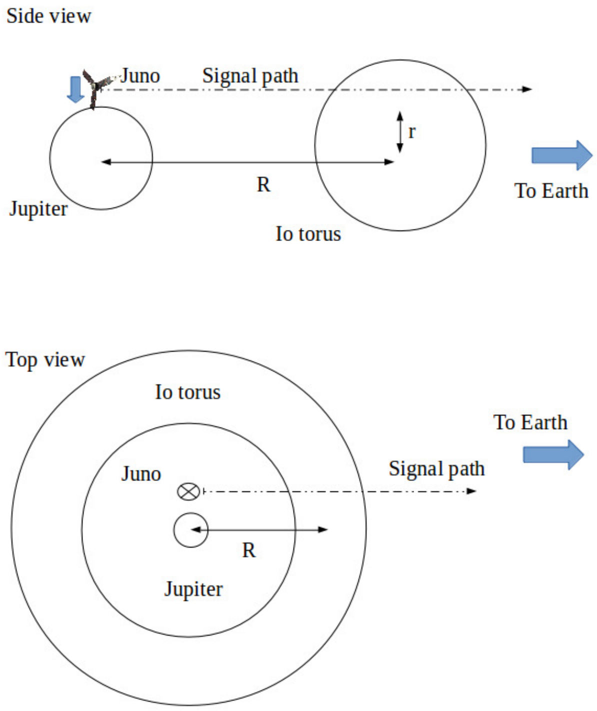

Figure 5. Schematic of the sophisticated model of the Io plasma torus and the geometry of an occultation. The electron density in the Io plasma torus is a function of the position coordinates r and R. (top) View from the dawn side of Jupiter with the Earth to the right. The arrow beside *Juno* shows the spacecraft's direction of motion. (bottom) View looking down on the north pole of Jupiter with Earth to the right. Here the *Juno* spacecraft is moving into the page.

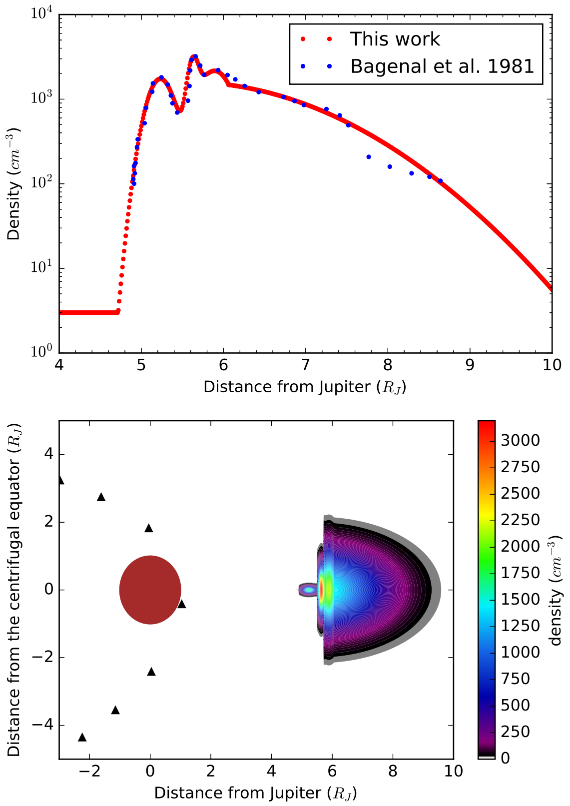

Figure 6. (top) Red symbols show electron densities in the plane of the centrifugal equator as a function of distance from Jupiter for the sophisticated model of the Io plasma torus. The innermost peak corresponds to the cold torus, the intermediate peak to the ribbon, and the outermost peak to the warm torus. The abrupt change in gradient at 6.1 R_J corresponds to the transition from the warm torus to the more distant extended torus. The blue points show *Voyager 1* data from *Bagenal and Sullivan* [1981]. (bottom) Colors indicate electron densities in the sophisticated model of the Io plasma torus. The red disk indicates Jupiter and the black triangles mark the position at one hour intervals of *Juno*, simulated by the University of Iowa ephemeris tool (www-pw.physics.uiowa.edu/∼jbg/juno.html).

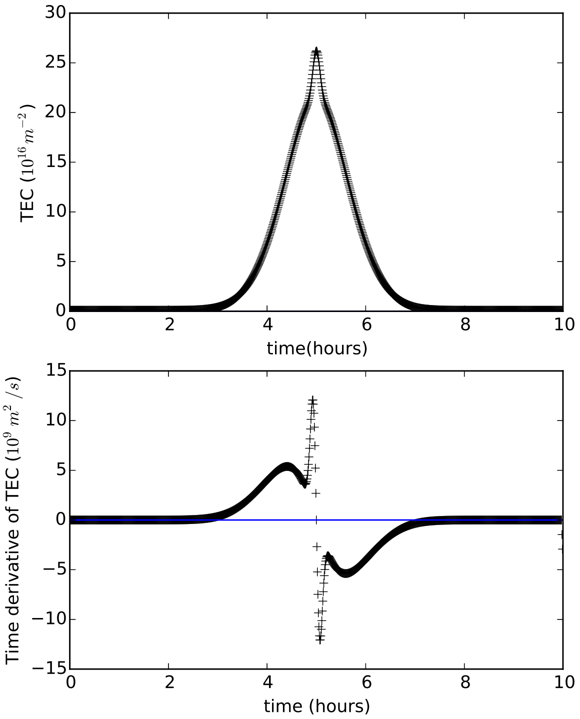

Figure 7. (top) Total electron content from the model shown in Figure 6 as function of time. At the start time, the spacecraft is approximately 4 R_J above the plane of the centrifugal equator. The subtle changes in the slope of the curve between 4 and 6 hours are signatures of the cold torus and ribbon. (bottom) Numerically calculated rate of change of the total electron content shown in the top panel.

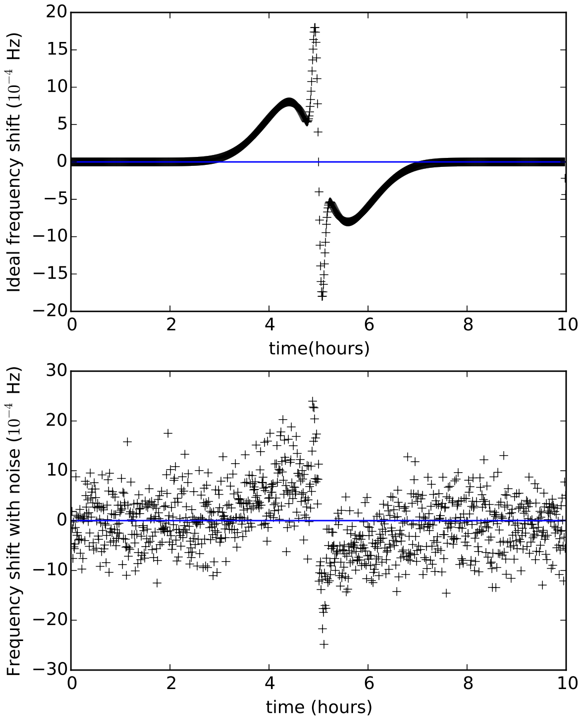

Figure 8. (top) Noise-free frequency shift calculated using Equation 4 and the rate of change of total electron content shown in the bottom panel of Figure 7 as function of time. (bottom) Same as top panel, but with noise added to the received frequencies.

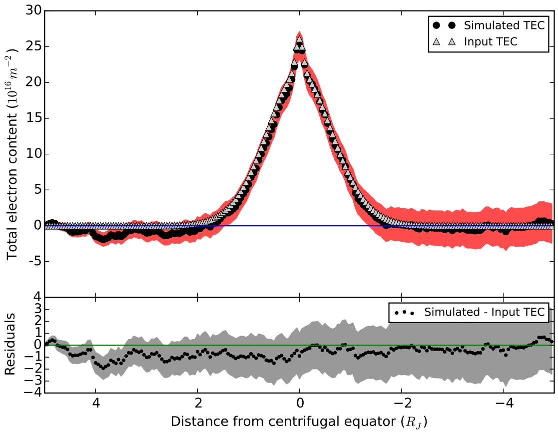

Figure 9. (top) The black points show the total electron content found by integrating the frequency shift in the bottom panel of Figure 8. The red shaded region is the uncertainty on the values. The gray triangles show the input total electron content values from the top panel of Figure 7. The blue line marks the location of zero. (bottom) The black symbols show the residuals between the simulated and the input total electron content. The gray shaded region marks the uncertainty on the residuals. The green line marks the location of zero.

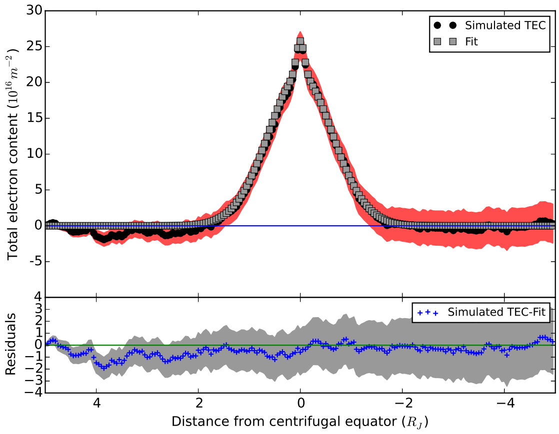

Figure 10. (top) The black points show the total electron content found by integrating the frequency shift in the bottom panel of Figure 8. The red shaded region is the uncertainty on the values. The gray squares show the MCMC fit to the integrated total electron content. The blue line marks the location of zero. (bottom) The blue plus signs show the residual between the fit and the simulated total electron content. The gray shaded region marks the uncertainty on the residuals. The green line marks the location of zero.

Table 1. *Juno* radio signal parameters [*Mukai et al.*, 2012]

Parameter		Value
Downlink Frequency [GHz]		
	X-Band	8.40413
	Ka-Band	32.0833
Turnaround Ratio		
	X to X-Band	$\frac{880}{749}$
	X to Ka-Band	$\frac{3344}{749}$[a]
	$\frac{f_{D,X}}{f_{D,Ka}}$	$\frac{880}{3344}$

[a] Assumed to match Cassini radio system [*Kliore et al.*, 2004].

Table 2. Input parameters for Io plasma torus model.

Region	Central Density [cm^{-3}]	Scale Height [R_J]	Peak Location [R_J]	Width [R_J]
Cold Torus	1710	0.1	5.23	0.20
Ribbon	2180	0.6	5.60	0.08
Warm Torus	2160	1.0	5.89	0.32
Extended Torus	1601	1.0	5.53	1.88

The central density, peak location, and width of the regions are derived from Figure 6 of *Bagenal and Sullivan* [1981]. The scale heights are derived from Figure 12 of *Bagenal and Sullivan* [1981]. Observations from the *Galileo* and *Cassini* spacecraft suggest that the ribbon position changes over time, but in general the center is thought to be located between 5.5 and 5.9 R_J [*Thomas et al.*, 2004].

Table 3. Best fit parameters from the MCMC fit to the simulated TEC data.

Parameter	Region	Fit Value	Input Value
Central TEC [10^{16} m^{-2}]	Cold Torus	$4.67^{+0.32}_{-0.20}$	4.29
	Ribbon	$3.98^{+0.25}_{-0.21}$	3.79
	Warm Torus	$17.06^{+0.79}_{-0.83}$	17.17
Scale Height [R_J]	Cold Torus	$0.11^{+0.01}_{-0.01}$	0.10
	Ribbon	$0.65^{+0.03}_{-0.05}$	0.60
	Warm Torus	$0.98^{+0.06}_{-0.05}$	1.0
Reduced Chi-Squared	1.004		